

The Elastic Properties and Plastic Behavior of Two-Dimensional Polymer Structures Fabricated by Laser Interference Lithography**

By Taeyi Choi, Ji-Hyun Jang, Chaitanya K. Ullal, Melburne C. LeMieux, Vladimir V. Tsukruk,* and Edwin L. Thomas*

The elastic and plastic properties within a two-dimensional polymer (SU8) structure with sixfold symmetry fabricated via interference lithography are presented. There is a nonuniform spatial distribution in the elastic modulus, with a higher elastic modulus obtained for nodes (brightest regions in the laser interference pattern) and a lower elastic modulus for beams (darkest regions in the laser interference pattern) of the photopatterned films. We suggest that such a nonuniformity and unusual plastic behavior are related to the variable material properties “imprinted” by the interference pattern.

1. Introduction

An epoxy-based negative photoresist from the Novolak-resin family, named SU8, has become a common material for the fabrication of complex microelectromechanical (MEMS) structures because of its mechanical durability, thermal stability, and dielectric properties, combined with its easy processability.^[1–3] SU8 is easily spun from solution to form a uniform glassy transparent film on various substrates. Its chemical structure, with eight epoxy rings, allows fast thermal and light-initiated crosslinking, resulting in a rigid network polymer with excellent chemical stability. Various MEMS devices, such as microgears, microcoils and pumps,^[4,5] microvalves and grippers,^[6] microchannels and high-aspect-ratio beams,^[7–9] microcantilevers and tribological coatings,^[10,11] phononic and photonic crystals, and light waveguides^[12–15] have been recently fabricated from SU8. The yield strength and elastic properties of microfabricated structures are critical for the reliable performance of these microdevices. Current MEMS design assumes the preservation of the mechanical properties of materials within the microscopic parts of MEMS structures, with the elastic modulus remaining close to that measured for the bulk state.^[10] However, in practice, the damping of dynamic properties of some

microfabricated devices points toward a more complex distribution of elastic and viscoelastic properties.^[16]

To date, only a few studies have addressed the question of the resultant mechanical properties of SU8 under complex microfabrication conditions. Feng and Farris reported a value of 3.2 GPa for the in-plane tensile elastic modulus, and 5.9 GPa for the out-of-plane elastic modulus for UV-cured materials, with the ultimate strain reaching 8%.^[17] Reducing the post-exposure bake time resulted in a decrease in the crosslinking density and, thus, a lower elastic modulus (down to 0.7 GPa), with an increase in elongation-to-break (up to 30%).^[7,18] The glass-transition temperature of SU8 is 55 °C in the uncured state and increases to 230 °C for the fully cured material; a linear relationship has been found between the glass-transition temperature and crosslinking density, and the degree of conversion of the epoxy groups reached 90% for electron-beam (e-beam) curing.^[18,19]

The recent application of advanced optical microfabrication methods such as holographic or interference lithography (ITL) for the creation of complex 2D and 3D microstructures introduces questioning of the actual distribution of crosslinking density and, thus, the corresponding spatial distribution of mechanical and thermal properties within these structures.^[2,5] In accordance with the usual consideration of MEMS structures, current approaches simply treat these complex porous microstructures as a two-phase (polymer–air) composite with the properties of the epoxy material being identical to those of the corresponding bulk state.

In order to investigate the actual material properties of the complex photopatterned materials fabricated by ITL, here we focus on the elucidation of the spatial distribution of elastic and plastic properties of a relatively simple 2D microstructure. Using atomic force microscopy (AFM), we conducted high-resolution nanomechanical studies of a thin SU8 film that has a hexagonal pattern of cylindrical air holes fabricated using three-beam laser ITL. A spatial distribution of the local elastic modulus that can be directly related to the symmetry of the light-intensity distribution within the original interference pattern in the photoresist is found, with a higher elastic modulus

[*] Prof. V. V. Tsukruk, M. C. LeMieux
Department of Materials Science and Engineering
Iowa State University
Ames, IA 50011 (USA)
E-mail: vladimir@iastate.edu

Prof. E. L. Thomas, T. Choi, Dr. J.-H. Jang, Dr. C. K. Ullal
Institute of Soldier Nanotechnologies
Department of Materials Science and Engineering, MIT
Cambridge, MA 02139 (USA)
E-mail: elt@mit.edu

[**] We thank S. Kooi for technical assistance and A. D. Nolte for the buckling instability test. This research was supported by the U.S. Army Research Office through the Institute for Soldier Nanotechnologies, under Contract DAAD-19-02-D-0002 and AFOSR, Grant F496200210205.

observed at the nodes (brightest regions in the laser interference pattern). The extremely plastic behavior of the films in the course of their fracturing is related to the essentially composite nature of the 2D perforated films with a high crosslink density obtained at the nodes and low crosslink density at the beams (darkest regions in the laser interference pattern).

2. Results and Discussion

2.1. Uniform Thin Films

Uncured and cured uniform SU8 films (laser exposure with a dose close to ITL conditions followed by development without thermal hard-baking; see Experimental) fabricated here for comparative purposes show a very smooth surface topography with a root-mean-square (rms) microroughness of 0.3 nm for uncured films and 0.9 nm for cured films (measured within $3\ \mu\text{m} \times 3\ \mu\text{m}$ areas). This similarity demonstrates little surface alteration after the laser-beam exposure and curing procedure used in this study (Figs. 1a and 2a). No significant wrinkling of the polymer film after crosslinking indicates that very little shrinkage and insignificant residual stresses developed in the bulk SU8 material, as has previously been reported.^[20,21]

The surface distribution of the elastic-modulus data of the uncured SU8 film obtained using static AFM force volume micromapping with a spatial resolution of below $0.2\ \mu\text{m}$ shows a relatively uniform distribution, and an indentation depth that does not exceed 3 nm (Fig. 1b).^[22] The histogram of the surface distribution of the elastic modulus confirms the uniform spatial distribution, with virtually all values obtained in the range 500–1500 MPa and an average elastic modulus of about 1 GPa (Fig. 1c). This value is fairly close to that reported for bulk SU8 films from tensile experiments for bulk specimens, and confirms the virtually identical microscopic elastic response of the thin films studied here and the macroscopic elasticity of the bulk material.^[18]

The surface distribution of the elastic moduli obtained with microscopic spatial resolution (below $0.1\ \mu\text{m}$) for cured SU8 films is also very uniform (Fig. 2b). The standard deviation for different surface areas was well below 20 %, indicating the absence of any significant spatial and chemical inhomogeneities on the microscale, which can be generated by light-initiated crosslinking and chemical developing (Fig. 2c). However, the average elastic modulus after curing increased significantly compared with the uncured film, and reached 2–4 GPa (Fig. 2c). This value is fairly close to that obtained from macroscopic tensile experiments for bulk SU8.^[17]

Lateral compression of the films on an elastomeric substrate was used to investigate their buckling instability and make an independent evaluation of the in-plane macroscopic elastic modulus.^[23] Such a deformation produced a very uniform buckling pattern, with a spacing of 100–180 μm extending over several square centimeters of the SU8 films (Fig. 3). This spacing of the buckling pattern obtained from 2D fast-Fourier-transform (FFT) analysis of the deformed films was used for the independent estimation of the elastic modulus of the films (Fig. 3). The elastic modulus measured by the buckling method (2–3 GPa)

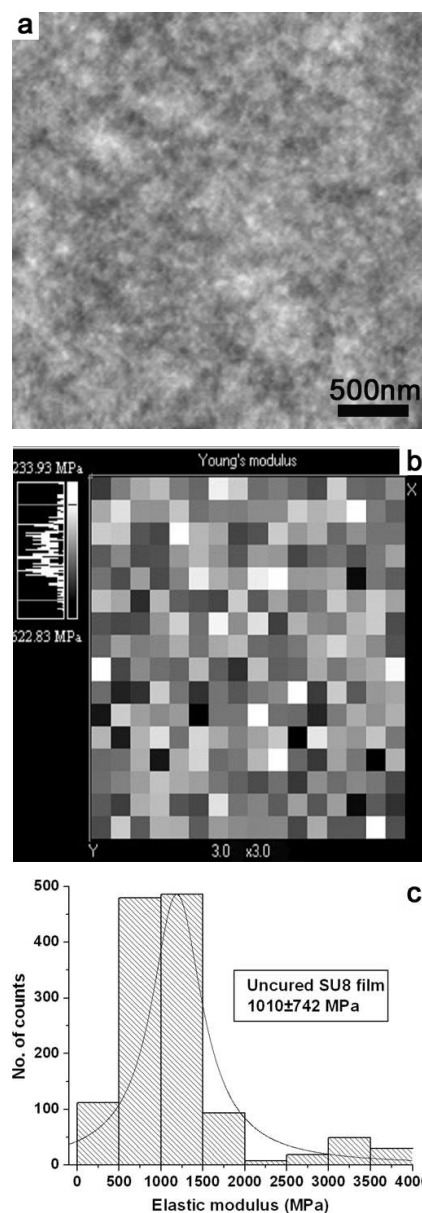


Figure 1. AFM data for an uncured SU8 film: a) AFM topography image; b) surface distribution of the elastic modulus ($3\ \mu\text{m} \times 3\ \mu\text{m}$); and c) histogram of the elastic-modulus distribution.

was similar to, but slightly higher than, those obtained from both AFM and macroscopic tensile measurements, which probably indicates differences related to the measuring routine of the in-plane compression of thin polymer films. Similarly, some higher elastic moduli have been recently measured for ultrathin multilayered polymer films in buckling experiments.^[24] However, despite some discrepancies in the absolute values, the buckling measurements confirmed the significant (by a factor of two to four) increase in the elastic modulus upon curing.

2.2. Microscopic Distribution of the Elastic Response

The interference pattern was designed to create a 2D lattice with hexagonal symmetry and predefined spacing and porosity.

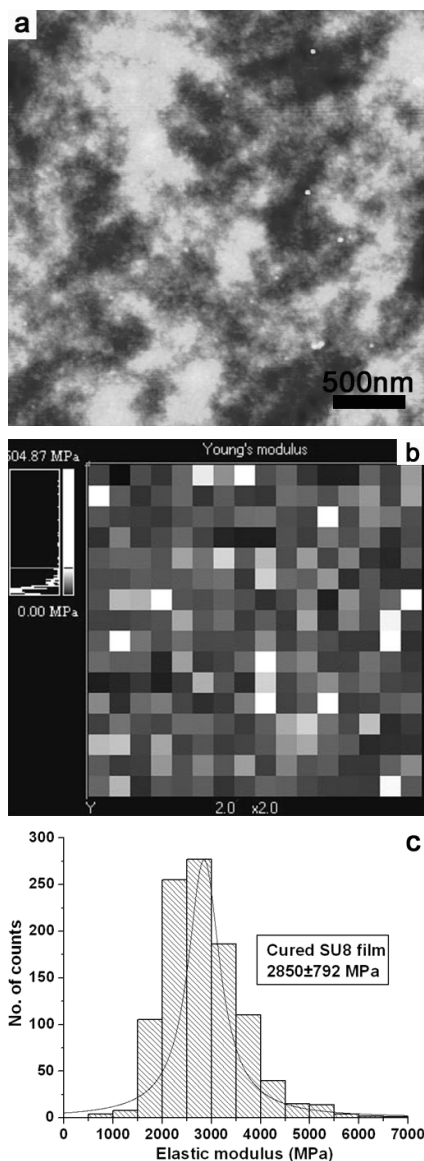


Figure 2. AFM data for a cured SU8 film: a) AFM topography image; b) surface distribution of the elastic modulus (2 μm x 2 μm); and c) histogram of the elastic-modulus distribution.

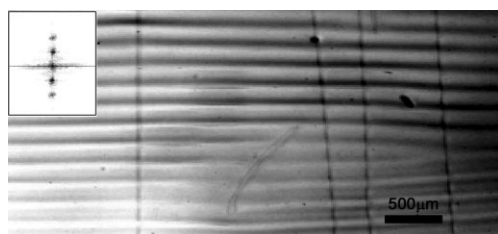


Figure 3. Elastic-buckling instability measurements of the uncured SU8 film on a poly(dimethylsiloxane) (PDMS) substrate. The buckling wavelength is 174 μm, as obtained from the inset Fourier-transform image.

The 2D distribution of light intensity created by three-beam interference is presented in Figure 4a, along with a sketch of the

unit cell and primary lattice vectors of the 2D lattice. The bright spots represent the nodes and the somewhat darker regions are the beams (as marked in Fig. 4a). The actual surface morphology of the photopatterned film shows a well-ordered, long-range, 2D lattice with a hexagonal array of air holes, closely resembling the theoretical light “template”, as can be seen in the scanning electron microscopy (SEM) image (Fig. 4b). The theoretical light distribution between nodes and beams is shown in Figures 4c and d, which show 1D intensity distributions along the [11] and [10] directions. The intensity of the light distribution along the [11] direction is a simple periodic function, although a more complex intensity distribution is observed along the [10] direction, with the intensity being slightly lower for beams between two neighboring nodes (Figs. 4c and d).

High-resolution surface morphology images of the 2D polymer films were obtained using tapping-mode AFM (Fig. 5). The AFM images reveal a well-developed topography with an array of round holes penetrating through the polymer film (Fig. 5a). A porosity level of about 40 % and a spacing of 1220 nm were estimated from the bearing analysis and 2D Fourier transforms of the AFM images, respectively. A diameter of the nearly cylindrical through holes of 700 nm was obtained from the AFM cross sections (see Fig. 5b, the shape is smeared by convolution with the AFM tip). The polymer surface between these round holes was relatively smooth, with the local microroughness not exceeding 1 nm within surface areas of 500 nm x 500 nm.

The nanomechanical measurements were conducted in the elastic regime, with an indentation depth of less than 2 nm allowing full elastic recovery of the tested surface areas after probing. The estimated contact area for a single nanoprobng experiment did not exceed 1 nm, which is much smaller than the distance between two consequential indentations (80 nm), thus precluding interference related to stress generation. High-resolution topographical images obtained simultaneously with nanomechanical probing, shown as a 32 x 32 array of small square pixels, are very similar to those obtained with conventional tapping-mode scanning (Fig. 6a). Each pixel in this image, with 80 nm x 80 nm lateral dimensions, represents the entire surface area for a single force measurement. In the course of the AFM micromapping, the AFM tip indented the surface in the center of this area, was pulled off, and moved to a neighboring surface area for the next nanoprobng.

The force–distance data obtained were converted to a loading curve (indentation vs. load) to evaluate the surface stiffness and elastic modulus by applying the Hertzian model of elastic deformation by a semispherical indenter interacting with a planar elastic solid. This approximation is acceptable for the small penetration depths and intermediate loading rates used in this work, as well as uniform surface morphology. Under these probing conditions, the viscoelastic contribution and auxiliary instrumentation contributions are negligible, as has been demonstrated for a variety of polymers in our previous publications.^[25–28] The application of the Hertzian approximation to AFM nanoprobng is based on the relationship between the normal pressure, P , and indentation depth, h , in the form of the equation^[29]

$$P = 4/3 R^{1/2} h^{3/2} E' \quad (1)$$

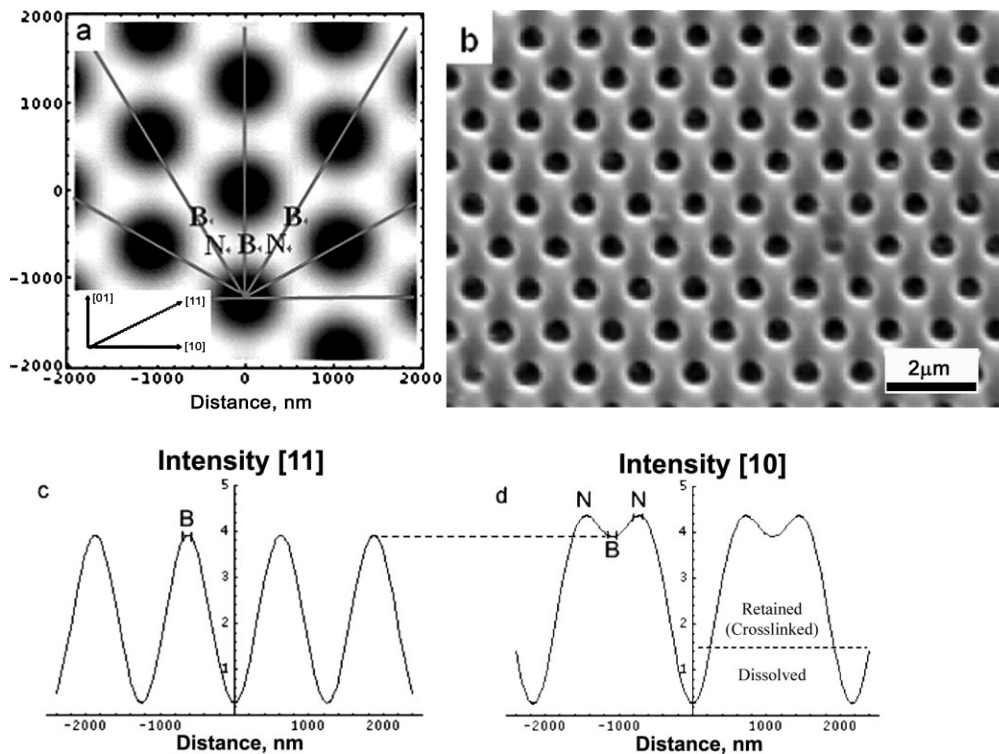


Figure 4. a) 2D light-intensity distribution for the three-beam interference used to fabricate the patterned specimen, along with the primary lattice vectors for the corresponding 2D lattice; B and N stand for regions of beams and nodes, respectively; inset shows primary lattice vectors. b) Scanning electron microscopy (SEM) image showing the long-range ordered 2D hexagonal lattice. c) 1D light-intensity distribution along the [11] direction (y axis in arbitrary values, DC offset is removed by amine). d) 1D light-intensity distribution along the [10] direction.

where R is the tip radius and E' is the composite modulus of the two contacting bodies. Thus, the composite elastic modulus (which is identical to the elastic modulus of the polymer for silicon tips) at an incremental depth (between $i-1$ and i) can be derived from

$$E_i = \frac{3}{4} (1 - \nu^2) \frac{k_n}{R^2} \frac{Z_{\text{defl},i,i-1}}{h_{i,i-1}^{3/2}} \quad (2)$$

where k_n is the normal spring constant of the cantilever, ν is Poisson's ratio, Z_{defl} is the incremental vertical deflection of the cantilever derived from the force–distance data and calibrated by the sensitivity measurement ($h = Z_{\text{pos}} - Z_{\text{defl}}$; Z_{pos} is the displacement of the AFM piezoelement).

The representative histogram of the elastic moduli for the surface area of the hexagonal patterned film (1024 force–distance curves collected over a $4 \mu\text{m} \times 4 \mu\text{m}$ area) showed a clear bimodal distribution of the elastic response (Fig. 6b). The spatial distribution of the surface stiffness (not shown) possessed very similar bimodal character. A broad distribution of moduli ranging from 300 MPa to 1.7 GPa corresponded to the wide distribution of the AFM probed locations (nodes, beams, sidewalls, and slope regions). Very low (close to zero) effective

modulus values were detected for the hole regions, with almost no resistance to the AFM tip. Underestimated values of “apparent” elastic modulus were also generated along the edges, where the actual slope of the surface corrupted the force probing because of side contact, a non-normal load, and the tip sliding instead of indenting. However, this type of topological contribution was significant only in the vicinity of the holes and inside the holes.

The surface distribution of the elastic moduli collected for larger surface areas of the patterned polymer film with lower resolution ($130 \text{ nm} \times 130 \text{ nm}$ per pixel) demonstrates the expected sixfold symmetry known from AFM imaging (Fig. 6c). A regular variation of the “apparent” elastic modulus on this spatial scale was determined by the surface topography, as is clear from the corresponding height and elastic modulus cross

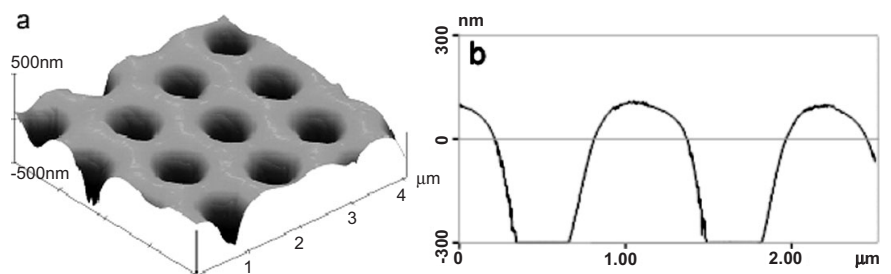


Figure 5. a) 3D surface topography of the specimen with an hexagonal pattern ($4 \mu\text{m} \times 4 \mu\text{m}$; tapping-mode AFM), and b) corresponding height profile along the [11] direction.

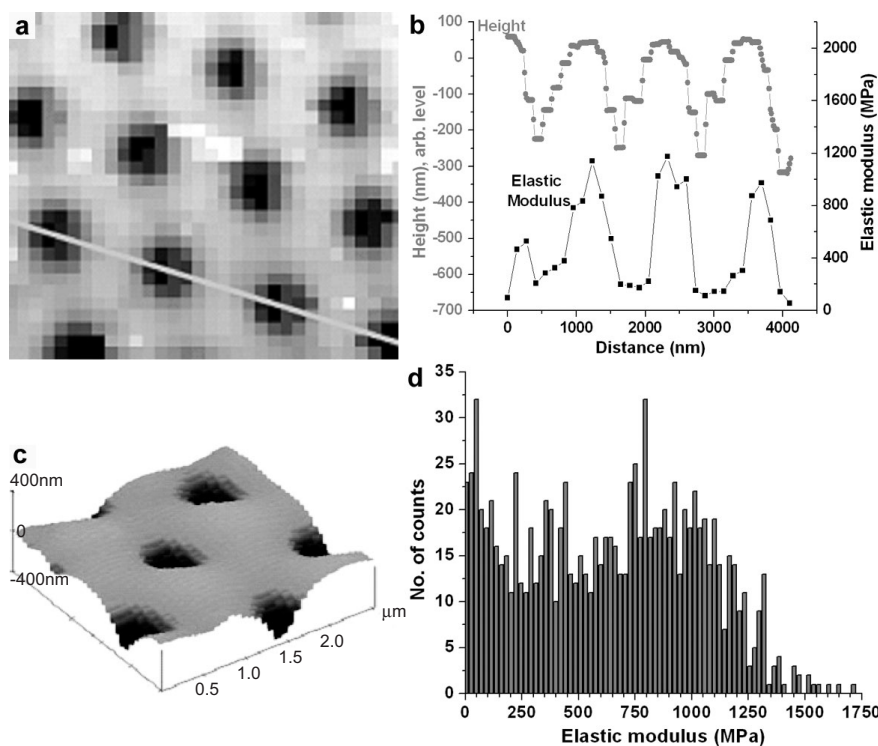


Figure 6. a) Top-view $4\ \mu\text{m} \times 4\ \mu\text{m}$ AFM topography image collected in force–volume mode with 32×32 resolution and b) corresponding height (compiled from a higher-resolution topographical image of this area) and elastic modulus cross-sections along the [11] direction (gray line in (a)). c) 3D topography of the surface areas mapped with 32×32 force spectroscopy ($2.5\ \mu\text{m} \times 2.5\ \mu\text{m}$). d) Surface distribution of the elastic modulus obtained from (c) (1024 data points).

sections along the [11] direction (Fig. 6d; gray line in Fig. 6c). The value of the elastic modulus is high and close to 2 GPa between holes, where the relatively flat polymer surface area was probed, but dropped to near-zero values inside the holes.

To address the question of the elastic-modulus distribution on the polymer surface on/between nodes and far from the holes, a higher-resolution micromapping (pixel size down to $60\ \text{nm} \times 60\ \text{nm}$) was implemented (Fig. 7). The selected surface areas, which included a complete set of nodes and beams with sixfold symmetry, were used to calculate the elastic moduli separately, for node and beam areas averaged over six locations (Figs. 7a and b). A statistically significant difference in the average elastic modulus between nodes and beams was derived from this analysis. Considering that the selected surface areas are reasonably flat (maximum slope angle was within 10°) the topological contribution can be neglected within the areas of interest. Given that the estimated contact area is only about 1 nm and that the potential tip sliding downhill should not exceed 20 %, we can essentially assume a spherical indenter on a plane with a small correction to the indentation, thus allowing the Hertzian model to be applied. Furthermore, adhesion histograms (not shown) did not show a significant gradient through this area, indicating a virtually constant contact area.

The difference between the elastic moduli for different locations was consistently observed for multiple nodes and beams probed independently (see dark and light gray areas in Fig. 7). On the other hand, we calculated the histogram of the elastic-modulus distribution for different smooth areas. We selected two surface areas representing beams and nodes that excluded the surface areas in the vicinity of the holes (Fig. 8a). For these areas, we calculated the statistical distribution of the elastic

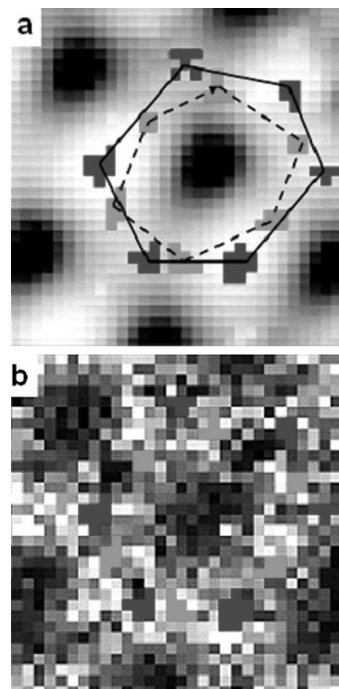


Figure 7. High-resolution AFM micromapping of the photopatterned SU8 film: a) 32×32 topography and b) elastic modulus collected during force micromapping of the $2.5\ \mu\text{m} \times 2.5\ \mu\text{m}$ surface area (two designated areas are marked by squares of pixels (dark gray for nodes and light gray for beams)).

moduli (Fig. 8b). The average elastic modulus obtained from these histograms for the nodes was 1480 ± 460 MPa, which is higher (beyond the standard deviation) than the calculated value for the beam areas, 1120 ± 590 MPa.

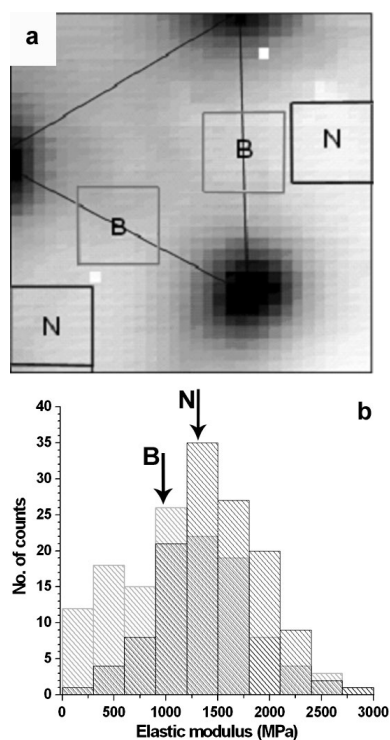


Figure 8. a) 32×32 high-resolution AFM topography image during force micromapping of a $2 \mu\text{m} \times 2 \mu\text{m}$ surface area, and b) combined surface histograms collected for selected surface areas ($500 \text{ nm} \times 500 \text{ nm}$) for nodes (black boxes) and beams (gray boxes).

We suggest that the observed location-dependent variation of the elastic moduli is caused by the spatial variation of the material properties “templated” by the light distribution within the interference pattern.^[30] The variable light distribution results in a variable crosslinking density, and, hence, the corresponding material properties, such as elastic modulus, glass-transition temperature, and plasticity behavior also vary.^[17,31,32] In ITL, the crosslinking density depends on both the dose and the distribution of the amine compensator. In fact, the almost-linear relationship between the illumination dose and the crosslinking density above the dissolution threshold was confirmed in this study by microprobing SU8 materials exposed to light doses from 0.38 to 3.8 J cm^{-2} (not shown). The 2D interference pattern produced a higher intensity in regions of constructive interference (nodes), with decreased intensity (down to zero) in regions of destructive interference (holes) (Fig. 4c). Regions with the highest intensity define lattice nodes with the highest crosslinking density (marked N in Fig. 4). The locations of holes (air holes after removing uncured material) correspond to the intensity minima, confirming the close correlation between the spatial distribution of intensity and the elastic-modulus distribution. The less-dramatic, but still significant, variation in the elastic modulus observed here for the beams and nodes of the photopatterned films also follows closely the light-intensity distribution in the interference pattern, reflecting a complex combination of spatial variation in crosslinking density, local glass-transition temperatures, and the amine-compensator distribution. The precise nature of the behavior observed will be addressed in future studies.

3. Conclusion

The 2D photopatterned films fabricated here can be considered as “natural” composite networks with potentially peculiar properties associated with the nonuniform distribution of internal elastic properties. In fact, in our preliminary studies, we observed very peculiar deformational behavior of these perforated films (Fig. 9). The SU8 film was fractured through external stresses by pulling the grafted film with sticky tape, and a variety of deformational modes were observed by SEM. In the two selected images presented here, one can see that the

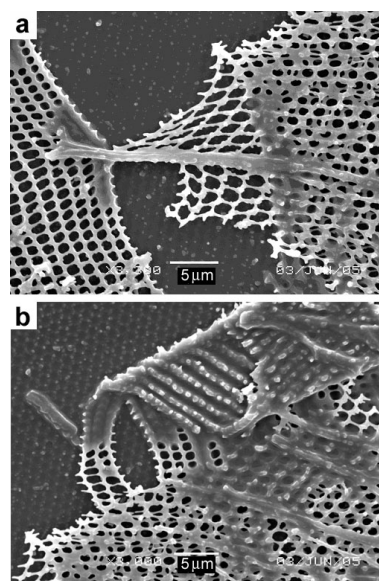


Figure 9. SEM images of a stretched and twisted polymer with a 2D hexagonal pattern, demonstrating extreme plasticity and unique fracturing behavior.

perforated SU8 films are capable of highly plastic behavior with significant local deformation of individual cells and large-scale deformation of the whole net (Fig. 9). High shearing and bending was observed for large film regions, which is completely uncharacteristic of glassy polymeric materials. Although this unusual behavior requires further investigation, we can speculate that precise control of the nonuniform internal elastic properties within ITL-microfabricated polymer structures makes these structures highly deformable and opens potential paths for photopatterned polymeric materials with efficient energy absorption on a sub-micrometer scale.

4. Experimental

2D patterns were fabricated using multibeam holographic ITL that allows generation of periodic structures over large areas with high resolution [33,34]. The fabrication procedure involved the interference of three equal-intensity laser beams and the transfer of the resultant intensity pattern onto an SU8 photoresist platform via laser-initiated cationic polymerization [35]. The materials platform consisted of Epon-SU8 (Shell) as a photoresist (a multifunctional epoxy derivative of a

bisphenol-A Novolac), cyclopentanone (Aldrich) as a solvent for spinning-on of the film, rubrene (Aldrich) as a photosensitizer that absorbs visible light and electron transfer to an onium salt, octoxyphenylphenyliodonium hexafluoroantimonate (OPPI) (UCB Radcure) as a photoacid generator, and tributylamine to compensate the nonzero background of the interference intensity. These compounds were first dissolved in cyclopentanone and then mixed with SU8 in a weight ratio of rubrene/OPPI/SU8 = 0.2:2:100, respectively. To increase the adhesion between the glass substrate and SU8 layer, a 1 μm thick buffer layer of SU8 was spin-coated (1 min, 2000 rpm) and baked (5 min, 95 °C). It was then flood-exposed under the UV lamp and hard-baked at 180 °C for 15 min. This layer effectively improved adhesion of the patterned SU8 layer to the substrate and prevented delamination during the developing process. Next, the SU8 solution in cyclopentanone was spin-coated on top of this existing SU8 film at a spin speed of 1000 rpm. The coated photoresist was then soft-baked at 95 °C for 10 min. The exposure was done using a 532 nm Nd:YAG (YAG: yttrium aluminum garnate) laser with an intensity of 0.3 W for 10 s to give a total exposure dose of 5–10 J cm⁻² over areas with diameters larger than 4 mm. After baking the 6 μm thick film at 65 °C for 5 min, the resultant cationic photopolymerization only took place in regions that were exposed to high intensities of light. The uncured regions were developed away in PGMEA (propyleneglycol monomethylether acetate) and the film was finally rinsed with isopropyl alcohol to yield the 2D porous photopatterned structure.

AFM studies were performed using a Multimode Nanoscope IV microscope (Digital Instruments, Inc.) [36]. Probing of the surface nanomechanical properties was conducted with static surface force spectroscopy using cantilevers with independently characterized spring constants (from 6 to 30 N m⁻¹) and tip radii (from 40 to 200 nm). Force–volume mode was applied to selected surface areas by collecting 32 × 32 point arrays of force–distance curves. The cantilever calibration, data processing, evaluation of the loading behavior (indentation depth vs. normal load), calculation of the surface stiffness and the elastic modulus by fitting loading curves, and the evaluation of the surface distribution of the elastic moduli were carried out in accordance with the usual approach by using the Hertzian contact mechanic model as described in detail previously [37,38]. Briefly, the AFM tip with known shape (deconvoluted by scanning a gold-nanoparticle reference specimen) indents the polymer surface with a probing frequency of 1 Hz. The indentation depth is selected to avoid any plastic deformations (within 2–4 nm for SU8 material). A nanoscale contact diameter within 1–2 nm limits the stress-field distribution to only several nanometers in the vicinity of the probed point, thus preventing the influence of consequential measurements and the presence of holes. The known bulk Poisson ratio was used for these calculations; possible deviation would not significantly affect the outcome of the calculations. The nanoscale structure of the SU8 films is considered to be uniform, and thus the model with local uniform distribution of the elastic modulus was applied for a single indentation within the 60 nm × 60 nm surface area. More complex models can be applied if evidence of a nonuniform nanoscale distribution is available, as discussed in a separate publication [38]. SEM images were obtained with a JEOL-6060 microscope. The strain-induced elastic buckling-instability measurements were carried out on uncured and cured SU8 films spun on the oxygen-treated poly(dimethylsiloxane) (PDMS) substrate [21,39].

Received: October 4, 2005

Final version: November 30, 2005

Published online: June 12, 2006

- [1] K. Y. Lee, N. LaBianca, S. Zolgharnain, S. A. Rishton, J. D. Gelorme, J. M. Shaw, T. H. Chang, *J. Vac. Sci. Technol. B* **1995**, *13*, 3012.
[2] G. Hong, A. S. Holmes, M. E. Heaton, *Microsyst. Technol.* **2004**, *10*, 357.

- [3] T. Staedler, K. Schiffmann, *Surf. Sci.* **2001**, *482*, 1125.
[4] H. Lorenz, M. Despont, N. Fahrni, N. LaBianca, P. Renaud, P. Vettiger, *J. Micromech. Microeng.* **1997**, *7*, 121.
[5] N. T. Nguyen, T. Q. Truong, *Sens. Actuators B* **2004**, *97*, 139.
[6] V. Seidemann, S. Bütetfisch, S. Büttgenbach, *Sens. Actuators A* **2002**, *97*, 457.
[7] H. Yu, O. Balogun, B. Li, T. W. Murray, X. Zhang, *J. Micromech. Microeng.* **2004**, *14*, 1576.
[8] H. Lorenz, M. Laudon, P. Renaud, *Microelectron. Eng.* **1998**, *41*, 371.
[9] R. G. Alargova, K. H. Bhatt, V. N. Paunov, O. D. Velev, *Adv. Mater.* **2004**, *16*, 1653.
[10] M. Calleja, J. Tamayo, A. Johansson, P. Rasmussen, L. M. Lechuga, A. Boisen, *Sens. Lett.* **2003**, *1*, 20.
[11] R. Bandorf, H. Lüthje, A. Wortmann, T. Staedler, R. Wittorf, *Surf. Coat. Technol.* **2003**, *174*, 461.
[12] T. Gorishnyy, C. K. Ullal, M. Maldovan, G. Fytas, E. L. Thomas, *Phys. Rev. Lett.* **2005**, *94*, 115 501.
[13] D. N. Sharp, M. Campbell, E. R. Dedman, M. T. Harrison, R. G. Denning, A. J. Turberfield, *Opt. Quantum Electron.* **2002**, *34*, 3.
[14] M. De Vittorio, M. T. Todaro, T. Stomeo, R. Cingolani, D. Cojoc, E. Di Fabrizio, *Microelectron. Eng.* **2004**, *73*, 388.
[15] M. Nathan, *Appl. Phys. Lett.* **2004**, *85*, 2688.
[16] F. E. H. Tay, J. A. V. Kan, F. Watt, W. O. Choong, *J. Micromech. Microeng.* **2001**, *11*, 27.
[17] R. Feng, R. J. Farris, *J. Mater. Sci.* **2002**, *37*, 4793.
[18] R. Feng, R. J. Farris, *J. Micromech. Microeng.* **2003**, *13*, 80.
[19] S. K. Rath, F. Y. C. Boey, M. J. M. Abadie, *Polym. Int.* **2004**, *53*, 857.
[20] A. Plepys, M. S. Vratsanos, R. J. Farris, *Compos. Struct.* **1994**, *27*, 51.
[21] K. K. Seet, V. Mizekis, S. Matsuo, S. Juodkazis, H. Misawa, *Adv. Mater.* **2005**, *17*, 541.
[22] S. A. Chizhik, Z. Huang, V. V. Gorbunov, N. K. Myshkin, V. V. Tsukruk, *Langmuir* **1998**, *14*, 2606.
[23] C. M. Stafford, C. Harrison, K. L. Beers, A. Karim, E. J. Amis, M. R. Vanlandingham, H. C. Kim, W. Volksen, R. D. Miller, E. E. Simonyi, *Nat. Mater.* **2004**, *3*, 545.
[24] A. J. Nolte, M. F. Rubner, R. E. Cohen, *Macromolecules* **2005**, *38*, 5367.
[25] V. V. Tsukruk, Z. Huang, S. A. Chizhik, V. V. Gorbunov, *J. Mater. Sci.* **1998**, *33*, 4905.
[26] V. V. Tsukruk, V. V. Gorbunov, Z. Huang, S. A. Chizhik, *Polym. Int.* **2000**, *49*, 441.
[27] A. Kovalev, H. Shulha, M. LeMieux, N. Myshkin, V. V. Tsukruk, *J. Mater. Res.* **2004**, *19*, 716.
[28] V. V. Tsukruk, V. V. Gorbunov, *Probe Microsc.* **2002**, *2*, 241.
[29] V. V. Tsukruk, A. Sidorenko, V. V. Gorbunov, S. A. Chizhik, *Langmuir* **2001**, *17*, 6715.
[30] C. Decker, T. N. T. Viet, D. Decker, E. Weber-Koehl, *Polymer* **2001**, *42*, 5531.
[31] J. Zhang, M. B. Chan-Park, S. R. Conner, *Lab Chip* **2004**, *4*, 646.
[32] L. Simonin, J. J. Hunsinger, J. P. Gonnet, D. J. Lougnot, *SPIE—Int. Soc. Opt. Eng.* **1996**, *2775*, 207.
[33] M. Campbell, D. N. Sharp, M. T. Harrison, R. G. Denning, A. J. Turberfield, *Nature* **2000**, *404*, 53.
[34] C. K. Ullal, M. Maldovan, G. Chen, Y. Han, S. Yang, E. L. Thomas, *Appl. Phys. Lett.* **2004**, *84*, 5434.
[35] S. Yang, M. Megens, J. Aizenberg, P. Witzius, P. M. Chaikin, W. B. Russell, *Chem. Mater.* **2002**, *14*, 2831.
[36] V. V. Tsukruk, *Rubber Chem. Technol.* **1997**, *70*, 430.
[37] J. L. Hazel, V. V. Tsukruk, *Thin Solid Films* **1999**, *339*, 249.
[38] H. Shulha, A. Kovalev, N. Myshkin, V. V. Tsukruk, *Eur. Polymer. J.* **2004**, *30*, 949.
[39] A. L. Volynskii, S. Bazhenov, O. V. Lebedeva, N. F. Bakeev, *J. Mater. Sci.* **2000**, *35*, 547.